Late-Holocene wind-field evolution at the southern Baltic coast as revealed by GPR data from the Mrzeżyno dunefield, NW Poland

Zuk, Tomasz; Sydor, Pawel; Sambrook-Smith, Greg

DOI:
10.1111/bor.12232

Late-Holocene wind-field evolution at the South Baltic Coast as revealed by GPR data from the Mrzeżyno dunefield, NW Poland

Tomasz Żuk, Paweł Sydor, Gregory H. Sambrook Smith

Dunefields usually show a similar response of all dunes to the wind regime. However, in the late-Holocene coastal dunefield in NW Poland the surface topography suggests that slipface orientation may vary significantly with distance from the coast, which is rarely reported in the literature. The dunefield was stabilised with forest in the mid-19th century preserving a unique record about atmospheric circulation in the South Baltic region at the end of the Little Ice Age. To elucidate the Holocene processes occurring along the study site a pseudo-3D GPR data set was collected. Six grids of parallel GPR lines combined with four hundred metres of GPR profiles (2D) were collected across the dunefield and displayed using GOCAD for interpretation and geostatistical analysis.

The geophysical data revealed that the larger aeolian forms are almost entirely formed by steeply laminated facies. Most importantly the pseudo-3D data, supported by geostatistical estimates of strata dip directions, revealed the existence of three zones parallel to the coastline with the mean dip direction almost perpendicular to the coast in the northern coastal strip and almost parallel to it in the southern part. Spreads of the dip directions in pseudo-3D GPR datasets recorded on the stoss slopes of dunes and crests suggested initial deposition on transverse dunes, which later were transformed into barchanoid dunes. This can probably be linked to changes in the wind regime, i.e. reduction in velocity of the northern and northwestern winds leading to reduced sediment supply from the coast. While the data provides a new interpretation of Holocene dunefield dynamics at this site, it also suggests that the minimum number of pseudo-3D GPR grids required to establish general trends using

geostatistical analysis should be at least 10, while even more data would be needed at larger, or more complex dunefields.

Keywords: Ground Penetrating Radar, Baltic Sea coast, dunefield, sedimentary architecture, climate change

Tomasz Żuk (tomasz.zuk@pgi.gov.pl) and Paweł Sydor (pawel.sydor@pgi.gov.pl), Polish Geological Institute–National Research Institute, Pomeranian Branch, 20 Wieniawskiego St., 71-130 Szczecin, Poland

Gregory H. Sambrook Smith (g.smith.4@bham.ac.uk), School of Geography, Earth and Environmental Science, University of Birmingham, Edgbaston Birmingham B15 2TT, United Kingdom

Introduction

During most of its geological history, the Earth surface was not vegetated and aeolian processes prevailed (Brookfield, 2011). During the Phanerozoic, there were also periods when sand seas dominated large proportions of sedimentary basins leaving vast sedimentary records (McKee, 1979; Glennie et al., 1978; Blakey et al., 1988; Kocurek, 1996). However, despite their importance the facies models of aeolian sandstones are oversimplified (Ahlbrandt and Fryberger, 1982; Rodríguez-López et al., 2014), and aeolian sediments are often assumed to be very homogenous and isotropic. This represents a significant knowledge gap as it is known that such deposits are associated with complexities at a range of different scales. As Fryberger and Hern (2014) summarised, the heterogeneity of aeolian deposits is evident at the (1) global (related to climatic cyclicity), (2) the basinal (stratigraphic formations and groups) and (3) the sub-basinal scale (intercalations with non-aeolian deposits), as well as at the local scale which includes (4) the outcrop/oilfield scale, associated with different properties of architectural elements such as dune and interdune deposits, and (5) the primary-strata scale, where heterogeneity of sediments stems from subtle textural changes.

This lack of detail about the internal heterogeneity of dunefields is also important from an applied perspective as aeolian deposits form important aquifers and hydrocarbon reservoirs (such as Permian Rotliegend in Netherlands, Germany, or Poland). The complexity of reservoirs formed by barchan dunes is mainly related to lateral anisotropy in permeability in steeply laminated facies (Prosser and Maskall, 1993). Krystinik (1990) found that anisotropy in permeability mostly varies with ratios between 4:1 and 25:1 with a significantly lower windward permeability produced by alternating cross-strata of different porosity. Thus, understanding variability in orientation of cross-strata across a dunefield is important to determine preferential pathways for fluid migration, which have a significant economic impact on management of aquifers, migration of contaminants and hydrocarbon reservoirs.

To meet these requirements for greater data resolution, GPR has become a very effective tool in imaging the internal organisation of individual dunes (e.g. Bristow et al., 2010). However, most of this data has been 2D sections which, without correlation with 3D data, cannot distinguish subtle changes (20–30°) of orientation in subsurface structures (Żuk and Sambrook Smith, 2015). Recently, Rodríguez-López et al. (2014, p. 1520) noticed that "3D GPR reconstructions of sedimentary architecture are rare", and "there exists a clear need for a comprehensive program of 3D GPR imaging of a representative selection of modern dunes to provide a 'library' of architectural styles for comparison with the rock record".

The present study is motivated by this requirement for more three-dimensional data, as articulated above, to then reveal more about aeolian processes in different systems. The primary aim is thus to collect pseudo-3D data from the coastal dunefield near the town of Mrzeżyno in northwestern Poland to provide new insights on the Holocene conditions in this area. The dunefield was stabilised with forest in the mid-19th century preserving a unique record about atmospheric circulation in the South Baltic region at the end of the Little Ice Age. Barchan and barchanoid dunes typically have a uniform distribution of cross-strata dip directions across dunefields (Bagnold, 1941; McKee 1966, 1979; Elbelrhiti et al., 2008; Vackiner et al., 2012) suggesting a shared response off all dunes to the prevailing wind regime. This has also been noted in the rock record; for example Peterson (1988) and Rowe et al. (2007) traced the Pangaea's equatorial monsoonal wind regime over many hundreds of kilometres in the Western United States based on cross-strata inclination consistent from the Permian to the Jurassic. Anomalies were only recorded between former mountain ranges. The wind pattern can significantly change with the evolution of sedimentary basins as shown by Kiersnowski (2013) for the Polish Upper Permian Basin. The assumption of unidirectional cross-stratification which results from the shared response of dunes to the wind regime is known to be erroneous at the Mrzeżyno dunefield as the topography shows that the slipface

orientation changes with distance from the coast. In addition, the height of the dunes in the northern part is greater and their topography is much more complex than in the southern part, suggesting different depositional conditions.

A secondary, more methodological aim of this work, involves establishing a guideline to collect and analyse pseudo-3D GPR data to reveal heterogeneities, particularly to establish the distribution of strata dip directions across a dunefield dominated by barchans and barchanoid dunes. In planning GPR data acquisition, important information is how many data points, i.e. pseudo-3D datasets, are necessary to carry out a reliable estimate of strata dip directions. In such a way the data from our study site can be used to inform future radar surveys to enable more complete interpretations of aeolian process-product relationships, and ancient deposits.

Study area

The study site is a small siliciclastic dunefield (about 16 km^2) located at the retreating barrier coast of the Southern Baltic Sea between the towns of Mrzeżyno and Pogorzelica (Fig. 1). The dunefield was stabilised by forest in the mid-19^{th} century (Sydor, 2012). Historical maps indicate the lack of forest in the first half of the 19^{th} century (Arrowsmith A., 1812, Renner and Ehricht, 1849), and its appearance at the end of the 19^{th} century (Topographische Karte 1:25 000 (Meßtischblatt) Blatt: Karnitz, 1910, Kirchhagener Fichten, 1890, Robe, 1915).

The landscape preserved up to 30-metre-high barchanoid dunes (in the northern part) and barchans (mostly on the southern edge), which migrated onto a peat land associated with the Rega River valley. The groundwater table is currently at a depth of about 1.5–2 m (3–3.5 m above the mean sea level), although the base of the aeolian cross-stratified sequence is 6.5–10.0 m below the current groundwater level suggesting significant subsidence associated with compaction of the underlying organic and fine-grained deposits. Currently, an approximately

two metre-thick layer of very compressed peat underlies the whole dunefield with radiocarbon dates (^{14}C) indicating that the organic deposition ended in the early Subboreal (4.5 ky BP) in the northwestern part and in late Subatlantic (0.76 ky BP) on the southeastern edge of the dunefield (Sydor, 2012). Below the layer of peat, there is a several metre-thick sequence of early-Holocene lacustrine silt and fluvial sand which in turn is underlain by glacial till and fluvioglacial sand (Dobracki and Zachowicz, 1997; Dobracka, 2008).

Based on the data gathered between 1971 and 2000 by the Institute of Meteorology and Water Management (Koźmiński et al., 2007), winds from the west and northwest, i.e. from the Baltic Sea have the highest velocities. Such winds prevail during the cold season, i.e. October to March (Fig. 2). Thus the seasonal wind regime can be classified as wide unimodal in accordance with the classification of Fryberger and Dean (1979).

Vibrocoring at 18 locations, on the dune ridges and in the interdune depressions, was done in 2011 and 2012 (Sydor, 2012), i.e. two to three years before the GPR data was collected. Only those drilled in the interdune depressions reached the bottom of the aeolian sequence and penetrated into the organic deposits. The vibrocore locations are shown in Fig. 1. Grain size analysis showed a range between 0.20 and 0.32 mm uniformly distributed across the study area with a mean value of about 0.23 mm and standard deviation of 0.31 mm, indicating fine well sorted sand (Sydor, 2012). Grains were not rounded suggesting short sediment transport.

Methods

Both 2D and pseudo-3D GPR data was collected from barchanoid dunes and from a coastal foredune. True 3D GPR data requires equal increments between measurement points both in the x and y direction, i.e. survey step and distances between parallel lines, a sampling interval smaller than about a quarter wavelength (Nyquist sampling interval), and all data

needs to be processed together (Grasmueck et al., 2005). Pseudo-3D data is collected as a series of survey lines where the survey step does not have to be the same as the distance between survey lines; each 2D profile is processed individually before compilation and 3D visualisation. The most representative and accessible aeolian forms were selected, while individual 2D lines were collected in the directions perpendicular to the dune crests (Fig. 1) using RAMAC GPR by MÅLA with unshielded 100 MHz and shielded 250 MHz antennas. We aimed to reach the maximum possible penetration of 2D data in order to acquire images below the base of entire dunes, therefore used lower frequency antennae than for the pseudo-3D survey. Four 2D lines (total length of 1105 m) were collected starting from the stoss and moving towards the lee side of the dunes. In order to validate sedimentary structures identified in GPR datasets, eight trenches (Sydor, 2012) were excavated in the dunes (4 on stoss slopes and 4 on lee slopes immediately below dune ridges). The depth of trenches was about 1.2 m with a length of about 3 m. The trench locations are shown in Fig. 1 and an example, including photos of trench walls and measurements taken, is shown in Fig. 3.

Compared to profiles measured in the direction of foreset dip, significantly higher signal-to-noise ratio was noticed in contrast to profiles collected in the opposite direction. This is attributed to the antenna design of the shielded RAMAC GPR by MÅLA with the receiver being located in front of the transmitting antenna. Thus when data is collected in the direction opposite to the strata dip the signal has to be transmitted between many more interfaces between zones of contrasting dielectric properties, i.e. layers of sand.

Six pseudo-3D grids (Fig. 1) of closely spaced parallel lines were collected using 250 and 500 MHz shielded antennas. Higher frequency antennas were used in order to acquire detailed 3D images to supplement the 2D profiles; the grids were located along the 2D lines. Grids A1 and B2 were collected on dune ridges, while grids B1 and C1 were located on stoss slopes. Grid D1 was collected in a large excavation (possibly a sand pit) in a dune in order to

image aeolian architecture at the base of the dune. The base of the excavation was rectangular in shape with dimensions of 80 x 25 m exposing the bottom section of a large sand dune. The dimensions of pseudo-3D grids ranged from 5×5 m to 25×50 m, while the distances between parallel lines varied between 0.1 and 0.5 m. Thus, only part of the dataset fulfil the Nyquist sampling interval necessary to create a true 3D dataset (Grasmueck et al., 2005). Data had the best quality with steplengths less than 0.2 m. Where the water table was at a depth of about 20 m or more, the maximum depth of images was within a similar range as reported in the literature for 100–250 MHz antennas (Neal and Roberts 2001; Jol et al. 2003; Bristow, 2009; Vriend et al. 2012), i.e. around 25–30 m. In the interdune areas, however, where the water table was at a depth of about 1–2 m with the top of the peat at about 8–10 m depth, signal penetration was limited to about 15–18 m. Grid E1 was located on the ridge of a coastal foredune (Fig. 1).

Processing was done using the open source software package Seismic Unix (Stockwell and Cohen, 2002), and was limited to time-variable frequency filtering and simple time-power gain recovery (no automatic gain control). Topographic correction was carried out by extracting the elevation of traces along GPR profiles from airborne LIDAR data (resolution of 4 points/m^2). Mean signal velocities for time-to-depth conversion of 0.1 m/ns for the unsaturated zone and 0.06 m/ns for the saturated aeolian sand were established based on the depths to the groundwater table and the base of aeolian sand derived from vibrocores (Fig. 1). These values are consistent with values given in the literature for slightly damp sand and wet aeolian sand (Neal, 2004; Bristow, 2009). They were also applied during topographic correction; the topography of dunes was not altered in any part of the profiles, which proves that the mean velocities do not vary significantly both horizontally and vertically. Stolt migration was initially applied but abandoned because some parts of the images were distorted resulting in no significant improvement. However, the real strata inclination on all

images is 16% steeper than the apparent dips shown in the GPR profiles (based on the geometrical relation $\sin\alpha = \tan\beta$, where α is true reflector inclination and β is apparent inclination). This is caused by the fact that GPR profiles display the signal reflected from the closest interfaces as located directly below the antennas, while in reality the closest point on a dipping reflector is never located directly below. Individually processed 2D lines were compiled with Seismic Unix into pseudo-3D datasets and converted into SEG-Y format for visualisation and interpretation using Paradigm GOCAD modelling software (Mallet, 1989).

Interpretation of GPR data was carried out in accordance with the principles of radar stratigraphy (Beres and Heani, 1991; Gawthorpe et al., 1993; Huggenberger, 1993; Neal, 2004) which evolved from seismic stratigraphy (Mitchum et al., 1977) dealing with reflection patterns on seismic profiles. Radar stratigraphy involves classification of radar facies and surfaces based on pattern, continuity and strength of GPR reflections. Radar facies distribution was analysed quantitatively in terms of their proportions within dunes and cross-strata dip directions, based on their area in individual 2D GPR profiles.

The distribution of dip azimuths across the dunefield (Fig. 4) was estimated using Empirical Bayesian Kriging incorporated in ArcGIS software (Krivoruchko, 2012), and was based on semivariogram (mean differences between azimuths of strata inclination against distances between measurement locations). The data presented here does not fulfil Kriging requirements of normal distribution, entropy of values and stationarity. However, Empirical Bayesian Kriging generates variograms from which a new dataset of measurements, which better fulfils the method requirements, is simulated. This dataset is in turn used to create new variograms, and the process of adjusting is repeated multiple times.

Cross-strata dip directions were measured using time-slices visualised in GOCAD. In total 896 measurements were taken in six pseudo-3D GPR grids. Time slices were selected at an interval of 10 ns, i.e. every 0.5 m. In order to account for lateral variability of strata dip

direction related to the fact that crests are slightly sinuous, each of the time slices was divided into four quarters. One measurement represents the dominant dip direction in each quarter of a time slice.

Radar facies are not unique to any sedimentary processes, or even sedimentary facies, which means that they have to be analysed together with the dominant palaeotransport direction (Jol et al., 2003). Changes in orientation of structures can be fully investigated when 3D GPR representations are available; particularity when information from horizontal slices is used. Here, the radar facies and surfaces were classified based on their 3D appearance in pseudo-3D datasets, and they were extended to 2D profiles, where the orientation of sedimentary structures would otherwise be uncertain. Radar facies and surfaces with their 2D and 3D representations are described below and summarised in Table 1.

GPR data quality significantly decreased below the groundwater table, and facies data below the groundwater table were only interpretable at the edges of the dunes, therefore we adopted the groundwater table as the bottom boundary for quantification of facies proportions.

Results

Radar facies and surfaces

Three radar facies and two types of radar surface were identified (Fig. 5, Tab. 1) with a significant dominance of steeply inclined, tabular, continuous reflections, sometimes of increasing thickness with depth, described as radar facies 1. Based on information from pseudo-3D GPR data, these reflections dip only in directions ranging from northeast and east to south and southwest. Radar facies 1 represents 85.2% to 100% of dune deposits on 2D profiles (measured as the surface occupied above the water table). Radar facies 2 is characterised by subhorizontal, parallel, sometimes undulating, continuous reflections, which often follow the topography of the stoss slope, dipping slightly in the direction opposite to the

dip direction of the large-scale cross-stratification associated with radar facies 1. Radar facies 2 was also found below the base of the dune shown on profile C–C'. In total, radar facies 2 represents 0% to 14.8% of dune deposits on 2D profiles. Radar facies 3, i.e. subhorizontal and horizontal, undulating, low and medium amplitude reflections, was only found 6–8 m below the groundwater table, and was therefore not taken into account.

Two types of radar surfaces have been identified. Radar surface 1 is represented by horizontal, planar or slightly undulating, continuous, strong to medium amplitude reflections, which are present in lower parts of profiles and usually underlie radar facies 1 (marked with green lines in Fig. 5). Radar surface 2 is represented by inclined, undulating, often concave upwards reflections of medium amplitude (marked with red lines in Fig. 5).

Dip directions of dune strata

The inclination of strata measured in trenches excavated on lee slopes (Fig. 1 and 3) was up to 26° on stoss slopes which corresponds to angles of cross-strata inclination obtained from the GPR profiles (Figs. 6–8). Figure 9 shows the distribution of dip directions in various pseudo-3D grids together with the mean dip directions. Pseudo-3D GPR datasets showed that the cross strata is inclined to the south and southeast near the coast (grids B1, B2 and E1) with mean dip direction ranging from 138° to 176° (with standard deviations ranging within each dataset between 4.23° and 22.88°) (Fig. 9). Further inland, the mean dip direction is to the east (grids A1, C1, D1) with mean azimuths between 67° and 98° (standard deviation ranged between 1.24° and 10.28°). Similarly, cross-stratification identified in trenches was inclined to the northeast closer to the coast, while further inland to the east and north east.

Apart from the dip directions observed within the near-surface deposits in grid D1 collected from the dune excavation, this GPR dataset also imaged another cross-stratified set below radar surface 1, which was inclined to the south (mean direction of 176°) with standard

deviation of 31.26° which varied significantly from the dip direction of the strata overlying it (mean of 67° and standard deviation of 10.03°).

Mean dip directions from the pseudo-3D GPR datasets A1, B1, B2 and C1 (Fig. 9) were compared with the azimuths of respective 2D profiles collected perpendicular to the dune crests. For datasets B1 and C1, the difference between the mean dip directions measured in pseudo-3D datasets and the azimuths of respective 2D profiles was 0° and 2°. These two pseudo-3D datasets were collected on the stoss slopes, and the spread of dip directions was much lower in comparison with the pseudo-3D datasets collected from the crests, i.e. A1 and B2 (see discussion below). These datasets were associated with a much larger spread of dip directions, while the difference between the survey line orientation and the mean dip direction was 32° in A1 grid and 30° in B2 grid. The mean value of the difference between the azimuths of 2D lines and mean dip directions in four pseudo-3D datasets (grids A1, B1, B2 and C1) is about 13°. This allowed confidence in assuming a relative conformity between the values of the mean dip direction and the orientation of lee slopes, and hence to use LIDAR data in order to create an additional 29 measurement points based on the azimuths of lee slopes. These points were selected along the ridges of the highest dunes and along the coastal foredunes in order to increase the number of points necessary to test how much data is needed for geostatistical estimations.

Interpolation of the values of dip directions using the geostatistical method showed that the dunefield can be divided three distinct areas associated with different cross-strata orientation. The boundaries between these zones are parallel to the coastline (Fig. 4A). The northernmost coastal zone extends 0.6 km inland and is associated with a mean azimuth of strata inclination of 144° (standard deviation of 0.8°). The middle, transitional zone is associated with a dip direction of 126° (standard deviation of 30.9°). The area along the southern edge of the dunefield is the largest with a mean dip direction of 86° (standard

deviation of 18.1°). The strata dip to the east (southern part of study site) coincides with the contemporary highest wind velocity which prevails in the cold season (Fig. 2).

To determine the minimum number of measurement points, as well as their optimal distribution, required to predict the distribution of dip directions across the dunefield, the number of measurement points used for estimation was gradually reduced (Fig. 10). At first, 12 measurement points from the western and eastern edges of the dunefield were removed (Fig. 10B). In the next step, 5 points from the northern edge were removed (Fig. 10C), followed by 17 measurement points from the middle part (Fig. 10D-G). The accuracy of the model also gradually decreased, and the map based on 10 measurement points (Fig. 10G) calculated using Bayesian Empirical Kriging followed general trends, however, it did not show any local heterogeneity mainly related to dunefield topography. The smallest changes on the map occurred after removing samples from the western and eastern edge of the dunefield. The biggest reduction in the quality of the model happened when points at the northern edge were removed. In the model generated using 44 points, there are only 3 anomalies – one in the southern zone and two in the transitional zone – with an average error of 10°. In the model generated using 10 points and validated using all 44, 11 points did not fit to the distribution and the error was 26° on average (Fig. 4B).

Discussion

Radar facies 1 has been interpreted as cross-strata, produced by grainflow processes on the lee sides of dunes (Fig. 5). Down-dip thickening of cross-strata, particularly in the bottom parts of dunes, suggests the dominance of grainflow over grainfall deposition, which is also expected given the significant height of the dunes (Hunter, 1977). Deposits at the base of a sand dune were investigated in detail in a large excavation where an 83 m-long 2D profile and

a pseudo-3D GPR grid with dimensions of 40 x 20 m were collected (Fig. 6) to image in detail the base of dune deposits as well as the underlying strata. Here, inclined, tabular and continuous reflections classified as radar facies 1 were identified to a depth of about 8.5 m below the ground level. Radar facies 1 is divided by radar surface 1 into two separate units, the lower represents a 4 m-thick cross-stratified bed. The stratum was preserved due to settlement below the groundwater table due to compaction of underlying peat deposits under the weight of the sand dune. The aeolian origin of these cross-stratified deposits was confirmed by grain-size (uniform well sorted sand of the same grain size and sorting as the upper aeolian unit, lack of coarser-grained intercalations), grain-shape and mineral content analyses carried out on samples taken from vibrocores as well as paleogeographical context based on vibrocore data (Sydor, 2012). The upper aeolian unit is composed of fine sand (mean grain size between 0.22 and 0.24 mm) which is very well sorted (standard deviation between 0.21 and 0.28). The lower aeolian unit is composed of very similar deposits (mean grain size between 0.22 to 0.23 mm) which also are very well sorted (standard deviation of 0.25). Both units are dominated by angular grains of quartz (22.4 to 46.7% in the upper unit and 29.0 to 48.0% in the lower unit) and transitional frosted grains (16.8 to 34.1 in the upper unit and in the lower unit 21/5 to 38.0%). Other pseudo-3D GPR datasets collected from dunes did not image the aeolian deposits below the groundwater table. However, this individual result from the southern edge of the dunefield documenting transport to the south (i.e. cross-strata inclined to the south) suggests different depositional conditions in this part of the dunefield. In the overlying unit, cross-stratification is inclined generally to the east, thus in the past there was possibly a stronger influence of wind blowing from the north and northwest. The total spread of dip directions recorded on stoss slopes of dunes (grids B1 and C1) was 75°, while on dune crests (grids A1 and B2) it was 140°. In grid D1 collected from the dune excavation in the southeastern part the spread of dip inclinations was 170°. Ahlbrandt and Fryberger

(1979) recorded a mean spread of 90° as typical for transverse dunes, with 180° recorded from barchans. Foresets found on stoss slopes were probably deposited on transverse dunes which later evolved into barchans and barchanoid dunes. This may potentially indicate the evolution of dunes driven by the changing wind regime and hence also the sediment supply. Transverse dunes typically form on sand sheets where the sediment source is dispersed, while barchans are more common in sediment starved areas with more focused sediment sources (Bagnold, 1941). Such a situation has been described by many authors (including McKee, 1979; Pye and Tsoar, 2009; Raffet et al. 2010). Minor vegetation could have played an important role in limiting sediment supply, however, it would result in formation of parabolic rather than barchanoid dunes. Within each dataset, the shape and orientation of cross-strata varies slightly with depth, although changes in dip direction are gradual with no rapid shifts. Thus, spread in dip direction measured in pseudo-3D GPR datasets should be related mostly to sinuosity of dune crests, rather than the presence of reactivation surfaces resulting from changes in transport direction.

Radar facies 2 is interpreted as upwind accretion. It represents erosional surfaces of secondary aeolian bedforms climbing up the dunes, or topsets. Topsets may include translatent wind-ripple lamination, i.e. subhorizontal laminae representing erosional surfaces left by migrating ripples (Hunter, 1977). Usually such stratification dominates forms smaller than 1.0 m (Hunter, 1977; Kocurek and Dott, 1981). The morphology of stoss slopes shown on profiles A–A’ and C–C’ (Figs. 4 and 6) where radar facies 2 are present also indicates small, up to 1 m high forms climbing the complex dunes. This radar facies could also represent lamination left by grainfall processes triggered by occasional events of strong wind blowing in directions opposite to the general dune migration, however, these forms have been recognised on the whole length of stoss slopes. Radar facies 2 below the base of the dune

shown on profile C–C’ is interpreted as small dome dunes similar to those found in the northern parts of the dunefield.

Radar surface 1 is interpreted as the erosional base of cross-stratified dune deposits or interdune surface (Kocurek, 1996), described by Brookfield (1977) as the first-order bounding surface. It is formed due to wind erosion of stoss slopes in scours between migrating dunes. The lower boundary of the aeolian deposits was also classified as radar surface 1. Based on the vibrocores drilled in the interdune areas, radar surface 1 at a level of 5 m above sea level on transect B–B’ is associated with the lithological boundary between fine and medium sand, while radar surface 1 at about 7.5 m below sea level at the start of the profile is associated with the boundary between aeolian sand and peat. Its inclination to the south is caused by a higher compaction of peat below the central part of the dune. The water table is now significantly above the bottom boundary of cross-stratified aeolian deposits, sometimes even over 10 m above it. Peat was identified at the GPR grid location with vibrocoring which reached a depth of 10.2 m, penetrating 1.7 m into the stratum. A distinct horizontal radar surface was also found at a depth of 17–18 m (Fig. 6), and based on historical boreholes from the area it is believed to represent the top of glacial till, confirmed by diffraction hyperbolas probably related to the presence of cobbles or boulders.

Radar surface 2 is interpreted as reactivation surfaces (Kocurek, 1996) produced by changes in wind direction which result in erosion of lee slopes of dunes, described by Brookfield (1977) as third-order bounding surfaces. According to Guillemoteau et al. (2012) third-order bounding surfaces are apparent on GPR profiles due to strong contrasts in grain size. Gradziński et al. (1979, 1986) pointed out that apart from the first to third order bounding surfaces, there are also erosional surfaces representing blowout structures in complex aeolian forms. These surfaces should be flat, or slightly concave upwards, and were identified on GPR profiles by Bristow et al. (2005). Here, they separate radar facies 1 from

radar facies 2, and were also classified as radar surface 2. Guillemoteau et al. (2012) relates the origin of these concave upwards reflections to contrasts in compaction between underlying and overlying sediments. Higher compaction of underlying sediments is caused by wind activity and bimodal distribution of grain sizes. i.e. two distinct grain-size populations, in the top few centimetres of sediments

2D GPR profiles showed mostly erosional surfaces of various orders including horizontal and subhorizontal translatent strata (radar facies 2), steeply inclined erosional surfaces created by avalanching of sand on lee faces (grain-flow, radar facies 1), reactivation surfaces (radar surfaces 2) as well as horizontal interdune surfaces and major lithological boundaries (radar surfaces 1). They also showed that the proportions of aeolian facies are relatively consistent across the study site. Although 2D data provided valuable information about potential complexity of sedimentary architecture, pseudo-3D data allowed the reliability of information based only from 2D profiles to be properly assessed. The orientation of the contemporary dune crests varied from the orientation of the cross-strata strike with a mean value of about 13° and a maximum difference of 33°. Time slices available in pseudo-3D GPR datasets were necessary to provide quantitative information about orientation of cross-strata and bounding surfaces as well as their lateral variability providing information about sinuosity of cross strata.

The geostatistical analysis which was carried out to show how much data is needed to determine distribution of dip directions involved the gradual reduction of the number of data points (GPR datasets, trenches, orientation of lee slopes) used to estimate the distribution of strata dip directions of uniformly cross-stratified deposits across the study area. It showed that the location of sampling points is equally important to their number. During removal of the measurement points, the accuracy of the map was more affected when points in the northern part of dunefield were removed than when points in the western and eastern parts of

dunefield were taken out. This suggests that the sampling points should be distributed along the main trend line cutting the middle of the area and along a line perpendicular to it. This test shows that the minimum number of samples (i.e. GPR datasets, trenches and dip directions assumed based on topography) is 10, although more than 30 points are required to show local anomalies. The optimum distribution required for this minimum number of 10 over an area of 16 km^2 to be sufficient to show general trends in strata dip directions in modern settings is when points are aligned along the main trend line as well as perpendicular to it. Kriging is based on semivariogram, thus a minimum number of sampling points cannot be reduced below a critical value. Smaller areas would still require the same number of data points, while larger, or more complex dunefields may require a larger amount of data.

Palaeowind directions are usually determined for sedimentary basins in order to reconstruct the character of aeolian reservoirs (Vackiner et al., 2012). The data presented herein can be referred to studies of simple rock reservoirs composed mostly of cross-stratified aeolian deposits resulting from migration of barchans and barchanoidal dunes (Al-Masrahy and Mountney, 2015). However, at the Mrzeżyno dunefield, the southern and northern zones have very different strata dip directions, with a difference in the mean values of 58° (144° in the northern and 86° in the southern zone). A similar distribution of dip directions was reported from Late Pleistocene coastal aeolianites in the Gaza Strip, Palestine by Zaineldeen (2010), where strata inclination changes both laterally over kilometre distance from the coast as well as vertically indicating that the wind pattern changed together with the distance to the shoreline (marine transgression).

As Eastwood et al. (2012) pointed out, the average dip direction of cross-strata can be assumed to be parallel to the wind direction when the wind regime is unidirectional. Here, the mean cross-strata dip azimuths are within a range of 110° which corresponds with the wind directions associated with highest mean velocities for the cold season, i.e. October to March

(Fig. 2). Large-scale cross-strata are only inclined in directions ranging from NE and E to SE and S. In contrast, the mean wind velocities are the lowest from the E, SE and S both during the cold and warm seasons. The most turbulent peaks, i.e. storms happening between October to March, are associated with north-western and north-eastern winds (Majewski, 2005).

Dip directions vary between three zones running parallel to the coast with azimuths perpendicular to the coast near the shore (yellow and red zones on Fig. 4A) and gradually changing to parallel to the coast further inland. This could be interpreted as a result of past changes in the wind regime. Currently, the highest mean velocities of wind are from the southwest and west (Fig. 2), however, in the past the sand must have been supplied from the beach located immediately to the north and northwest of the dunefield. The topography suggests that the velocity of a northwestern wind is currently sufficient to form the coastal foredunes and rapidly decelerates near the coast. Transgressive parabolic dunes on the Wolin spit, white dunes described by Keilhack (1912) and Borówka et al. (1986) have been investigated using OSL dating by Reimann et al. (2011). These parabolic dunes migrated to the south and were deposited between 1540 and 1660 AD, i.e. during the Little Ice Age. Nevertheless, without reliable dating the age of the dunes in the northern part and the lower aeolian unit in the southern part of the Mrzeżyno dunefield is uncertain.

The evolution of the dunefield revealed by the analysis of quantitative information extracted from pseudo-3D GPR data as well as vibrocoring can be summarised in the following four stages (Fig. 11). Wetlands and small lakes existing during the 1st stage (Fig. 11A); the wet ground surface as well as vegetation could have initiated the aeolian accumulation. Based on the radiocarbon dating of the peat underlying the aeolian deposits, in the western part of dunefield, aeolian accumulation of horizontally laminated sand sheets (Fig. 11B) might have already started in the Early Subboreal (4.5 ky BP) and reached the southern and southeastern parts not earlier than in the Late Subatlantic (0.76 ky BP) (Sydor,

2012). Cross-strata dip directions in the lower layer in pseudo-3D GPR grid D1 (Fig. 5) suggest that during this time wind from the northwest and north must have played a much more important role delivering sand from the beach to the whole dunefield and producing cross-stratification inclined to the south and southeast even in the southern zone. No OSL dates are available, however, analysis of transport directions within the near-surface cross-stratified layer revealed that the later stage (3rd, Fig. 11D) of the dunefield evolution was associated with the decreasing influence of the northern and northwestern wind. During this phase, settlement of the organic deposits led to accumulation of sedimentary material redeposited by wind from the west and southwest. The cross-stratification of the more recent deposits is inclined to the east and northeast. This dominant transport direction is consistent with the contemporary directions of wind in the cold season (Fig. 2). The dunefield was stabilized by forest growth (Fig. 11E) in the mid-19th century as indicated by the historical maps. Future OSL dating should confirm the exact timeframe of the dunefield evolution.

Conclusions

The study based on pseudo-3D GPR datasets demonstrated that cross-stratified aeolian deposits can be associated with a significant lateral and vertical heterogeneity in strata dip directions. When datasets from the stoss slopes were compared with those collected from the dune crests, transformation of depositional style, from transverse into barchanoid type, was revealed. Such evolution resulted from a decrease of sediment supply from the north and differentiation of the transport directions between the coastal strip and the southern zone which was sheltered from the north and more exposed to a westerly and south-westerly wind. This evolution was not influenced by increased vegetation, which would result in parabolic rather than barchanoid dunes. Three distinct zones with boundaries parallel to the coastline

associated with the mean strata dip directions varying by 58° between the coastal and southern strips were established using geostatistics.

The geostatistical modelling of strata dip directions showed that the optimum distribution of pseudo-3D GPR datasets at the site is when data locations are aligned parallel to boundaries between zones characterised by different depositional conditions as well as perpendicular to them with variable distances between them. The minimum number of sampling points required to establish general trends at the site using geostatistical analysis was 10. Because semivariograms need to be constructed, even if a dunefield is smaller and not as complex as this site, 10 points is still the minimum number. However, more data will definitely be needed when surveys are carried out at larger dunefields, or when the sedimentary architecture is more complex.

Acknowledgements. The project was funded by the statutory research grant of the Polish Geological Institute – National Research Institute No. 61.9101.1401.00.0. We would like to thank the Editor, Jan Piotrowski as well as the Reviewers Sebastian Lindhorst and Rajesh R. Nair whose valuable comments significantly improved the manuscript. We also would like to thank Paradigm for providing GOCAD software for data visualisation and interpretation.

Literature

Ahlbrandt, T.S., Fryberger, S.G., 1979. Eolian deposits in the Nebraska Sand Hills, U.S. Geological Survey Professional Paper 1120A, 1–24.

Ahlbrandt, T.S., Fryberger, S.G., 1982. Introduction to eolian deposits. In: Scholle, P. A., Spearing, D. (Eds.), Sandstone Depositional Environments: AAPG Memoir 31, pp. 11–47.

Al-Masrahy M.A., Mountney N.P., 2015. A classification scheme for fluvial-aeolian interaction in desert-margin settings. Aeolian Research 16, 67–88.

Arrowsmith A., 1812. Map of the Physical Divisions of Germany. London (scale ca. 1:490 000).

Bagnold R., 1941. Physics of Blown Sand and Desert Dunes, Mathuen, London, pp. 1–256.

Beres, M., Haeni, F.P., 1991. Application of ground-penetrating-radar methods in hydrogeologic studies. Ground Water 29, 375–386.

Blakey, R.C., Peterson, F., Kocurek, G., 1988. Synthesis of late Paleozoic and Mesozoic eolian deposits of the Western Interior of the United States. In: Kocurek, G. (Ed.), Late Paleozoic and Mesozoic Eolian Deposits of the Western Interior of the United States. Sedimentary Geology 56, pp. 3–125.

Borówka, R.K., Gonera, P., Kostrzewski, A., Nowaczyk, B., Zwoliński Z. 1986. Stratigraphy of eolian deposits in Wolin Island and surrounding area, North-West Poland. Boreas 15, pp. 301–309.

Bristow, C., Lancaster, N., Duller, G.A.T., 2005. Combining ground penetrating radar surveys and optical dating to determine dune migration in Namibia. Journal of Geological Society of London 162, 315–321.

Bristow, C., 2009. Ground penetrating radar in aeolian sand dunes, In: Jol, H.M. (Ed.), Ground penetrating radar: theory and application. Elsevier Science, Oxford, pp. 273–297.

Bristow, C.S., Augustinus, P.C., Jol, H.M., Wallis, I.C., Rhodes, E.J., 2010. Topographic steering and dune morphology in a Polar desert, analogues for Mars from the McMurdo dry valleys of Antarctica. In: Second International Planetary Dunes Workshop, 2010, Alamosa, Colorado, USA, 1–2.

Brookfield, M.E., 1977. The origin of bounding surfaces in ancient eolian sandstones. Sedimentology 24, 303–332.

Brookfield, M.E., 2011. Aeolian processes and features in cool climates. Journal of Geological Society of London 354, 241–258.

Dobracka, E., 2008. Szczegółowa mapa geologiczna Polski w skali 1 : 50 000 scale, arkusz Niechorze (77) – objaśnienia. Polish Geological Institute, Szczecin.

Dobracki, R., Zachowicz, J., 1997. Mapa geodynamiczna polskiego wybrzeża Bałtyku w skali 1:10 000, arkusze Pogorzelica (9) and Mrzeżyno (10). Polish Geological Institute, Szczecin.

Eastwood, E.N., Kocurek, G., Mohrig, D., Swanson, T., 2012. Methodology for reconstructing wind direction, wind speed and duration of wind events from aeolian cross-strata, Journal of Geophysical Research 117.

Elbelrhiti, H., Andreotti, B., Claudin, P., 2008. Barchan dune corridors: Field characterization and investigation of control parameters. Journal of Geophysical Research 113, F02S15.

Fedorowicz, S., Zieliński, P., Wysiecka, G., Hołub, B., 2012. Phases of aeolian accumulation on the Vistula Spit (Southern Baltic Sea) in the light of TL dating and analysis of a digital elevation model. Geological Quarterly 56(2), 345–352.

Fryberger, S.G., Dean, G., 1979. A study of global sand seas: Dune forms and wind regime. U.S. Geological Survey Professional Paper, United States 1052, 137–169.

Fryberger, S.G., Hern, C.Y., 2014. A Geometric Approach to the Analysis of Global Eolian Hydrocarbon Reservoirs, Poster session at the AAPG-RMS, July 2014.

Gawthorpe, R.L., Collier, R.E.L., Alexander, J., Leeder, M., Bridge, J.S., 1993. Ground penetrating radar: application to sand body geometry and heterogeneity studies. Geological Society of London Special Publication 73, 421–432.

Glennie, K.W., Mudd, G.C., Nagtegaal, P.J.C., 1978. Depositional environment and diagenesis of Permian Rotliegendes sandstones in Leman Bank and Sole Pit areas of the UK southern North Sea, Journal of the Geological Society of London 135, 25–34.

Gradziński, R., Gągol, J., Ślączka, A., 1979. The Tumlin sandstone (Holy Cross Mts, Central Poland): Lower Triassic deposits of aeolian dunes and interdune areas. Acta Geologia Polonica 29, 151–175.

Gradziński, R., Kostecka, A., Radomski, A., Unrug, R., 1986. Zarys sedimentologii. Wydawnictwa Geologiczne, Warszawa, pp. 1–628.

Grasmueck, M., Weger, R., Horstmeyer, H., 2005. Full-resolution 3-D GPR imaging, Geophysics 70, K12–K19.

Guillemoteau, J., Bano, M., Dujardin, J.R., 2012. Influence of grain size, shape, compaction on georadar waves: example of an Aeolian dune. Geophysical Journal International 190, 1455–1463.

Hass, H.C., 1996. Northern Europe climate variations during late Holocene: evidence from marine Skagerrak. Palaeogeography, Palaeoclimatology, Palaeoecology 123, 121–145.

Huggenberger, P., 1993. Radar facies: recognition of facies patterns and heterogeneities within Pleistocene Rhine gravels, NE Switzerland. Geological Society of London Special Publication 75, 163–176.

Hunter, R.E., 1977. Basic types of stratification in small eolian dunes, Sedimentology 24, 361–387.

Jol, H.M., Bristow, C.S., Smith, D.G. Junck, M.B., Putnam, P., 2003. Stratigraphic imaging of the Navajo Sandstone using ground-penetrating radar. Leading Edge 29, 882–887.

Keilhack, K., 1912. Die Verlandung der Swinepforte. Jahrbuch der Königlich Preussischen Geologischen Landesanstalt, pp. 32, 209–244.

Kiersnowski, H., 2013. Late Permian aeolian sand seas from the Polish Upper Rotliegend Basin in the context of palaeoclimatic periodicity, Geological Society of London Special Publications 376, 431–456.

Kocurek, G., 1996. Desert aeolian systems. In: Reading, H.G. (Ed.), Sedimentary Environments: Processes, Facies and Stratigraphy. Blackwell Science, Oxford, pp. 125–153.

Kocurek, G., Dott, Jr. R.H., 1981. Distinctions and uses of stratification types in the interpretation of eolian sands. Journal of Sedimentary Petrology 51, 579–595.

Koźmiński, C., Michalska, B., Czarnecka, M., 2007. Klimat województwa zachodniopomorskiego, Akademia Rolnicza w Szczecinie, Uniwersytet Szczeciński, Szczecin pp. 1–147.

Krivoruchko, K., 2012. Empirical Bayesian Kriging, ArcUser Fall 2012, 6–10.

Krystinik, L. F., 1990. Development geology in eolian reservoirs. In: Fryberger, S.G. Krystinik, L.F., Schenk, C.J., (Eds.), Modern and ancient eolian deposits. Petroleum Exploration and Production The Rocky Mountain Section SEPM, Denver, Colorado, 135–146.

Mallet, J. L., Jacquemin, P., Cheimanoff, N. 1989. GOCAD project: Geometric modeling of complex geological surfaces. Technical Program Expanded, Society of Exploration Geophysicists.

McKee, E.D., 1966. Structures of dunes at White Sands National Monument, New Mexico (and a comparison with structures of dunes from other selected areas), Sedimentology 7, 3–69.

McKee, E.D., 1979. Sedimentary structures in dunes. U.S. Geological Survey Professional Paper 1052, 137–169.

Mitchum, J.R., Vail, P.R., Sangree, J.R., 1977. Seismic stratigraphy and global changes of sea level, Part 6: Stratigraphic Interpretation of Seismic Reflection Pattern. In: Payton, C.E. (Ed.), Seismic stratigraphy—applications to hydrocarbon exploration. American Association of Petroleum Geologists Memoir 26, 117–133.

Neal, A., 2004. Ground-penetrating radar and its use in sedimentology: principles, problems and progress. Earth-Science Reviews 66, 261–330.

Peterson, F., 1988. Pennsylvanian to Jurassic Eolian transportation systems in the Western United States. In: Kocurek, G., (Ed.), Late Paleozoic and Mesozoic Eolian Deposits of the Western Interior of the United States. Sedimentary Geology 56, 207–260.

Prosser, D.J., Maskall, R., 1993. Permeability variation within aeolian sandstone: a case study using core cut sub-parallel to slipface bedding, the Auk Field, Central North Sea, UK. In: North, C.P., Prosser, D.J. (Ed.), Characterisation of fluvial and aeolian reservoirs, Geological Society Special Publication 73, 377–397.

Pye K., Tsoar H., 2009. Aeolian Sand and Sand Dunes, Springer, Berlin, pp. 1–476.

Reffet, E., S. Courrech du Pont, S.R., Hersen, P., Douady, S., 2010. Formation and stability of transverse and longitudinal sand dunes. Geology 38, 491–494.

Reimann, T., Tsukamoto, S., Harff, J., Osadczuk, K., Frechen, M., 2011. Reconstruction of Holocene coastal foredune progradation using luminescence dating - An example from the Świna barrier (southern Baltic Sea, NW Poland). Geomorphology 132, 1–16.

Renner, L., Ehricht, C., 1849. Provinz Pommern 1849. Bibliographishes Institut, Hildburghausen.

Rodríguez-López, J.P., Clemmensen, L.B., Lancaster, N., Mountney, N.P., Veiga, G.D., 2014. Archean to Recent aeolian sand systems and their sedimentary record: Current understanding and future prospects. Sedimentology 61, 1487–1534.

Rowe, C., Loope, D.B., Oglesby, R.J., Van der Voo, R., Broadwater, C.E., 2007. Inconsistencies between Pangean reconstructions and basic climate controls. Science 318, 1284–1286.

Stockwell, J.W., Jr., Cohen, J.K., 2002. The new SU user's manual. Center for Wave Phenomena, Colorado School of Mines, Golden, Colorado, USA

Sydor, P., 2012. Wykształcenie i wiek wydm w północno-zachodniej Polsce na przykładzie pola wydmowego w rejonie Pogorzelicy (unpublished report from project: Geneza i zmiany lini brzegowej wybrzeża trzebiatowskiego u schyłku glacjału i w holocenie w świetle badań paleogeograficznych). Polish Geological Institute - National Research Institute, Szczecin, pp. 1–31.

Topographische Karte 1:25 000 (Meßtischblatt) Blatt: Karnitz, 1910.

Topographische Karte 1:25 000 (Meßtischblatt) Blatt: Kirchhagener Fichten, 1890.

Topographische Karte 1:25 000 (Meßtischblatt) Blatt : Robe, 1915.

Uścinowicz, Sz., 2003. Relative sea level changes, glacio-isostatic rebound and shoreline displacement in the Southern Baltic. Polish Geological Institute Special Papers 10, 1–80.

Vackiner, A., Antrett, P., Strozyk, F., Stollhofen, H., Back, S., Kukla, P., 2012. Reconstructing the Upper Permian sedimentary facies distribution of a tight gas field in Central Europe on the basis of an analog field study in the Panamint Valley, western U.S. Geosphere 8, 1129–1145.

Vriend, N.M, Hunt, M.L., Clayton R.W., 2012. Sedimentary structure of large sand dunes: examples from Dumont and Eureka dunes, California. Geophysical Journal International 190, 981–992.

Zaineldeen, U.F., 2010. Paeowind estimation of cross-bedding with the aeolian Kurkar layers of the Gaza Formation, Gaza Strip, Palestine. Geologia Croatica 63, 55–65.

Żuk, T., Sambrook Smith, G.H., 2015. Radar stratigraphy – a method for analysing 3D GPR data in sedimentary environments as exemplified by fluvial sediments. Przegląd Geograficzny 87, 439–456.

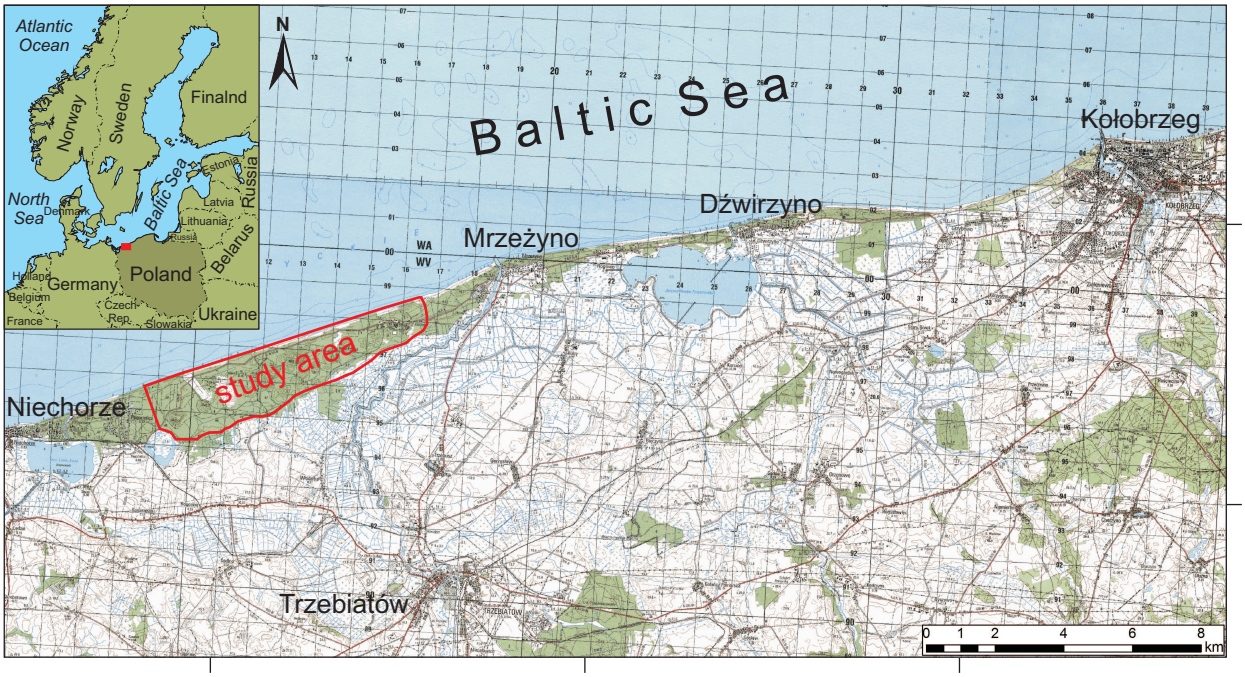
Atlantic Ocean
Norway
Sweden
Finalnd
North Sea
Denmark
Baltic Sea
Estonia
Latvia
Lithuania
Russia
Belarus
Poland
Germany
Ukraine
Czech Rep.
Slowakia
France
Belgium
Holland
N
Baltic Sea
Kołobrzeg
Dźwirzyno
Mrzeżyno
study area
Niechorze
Trzebiatów
0 1 2 4 6 8 km
54ş10'N
54ş05'N
15ş10'E
15ş20'E
15ş30'E

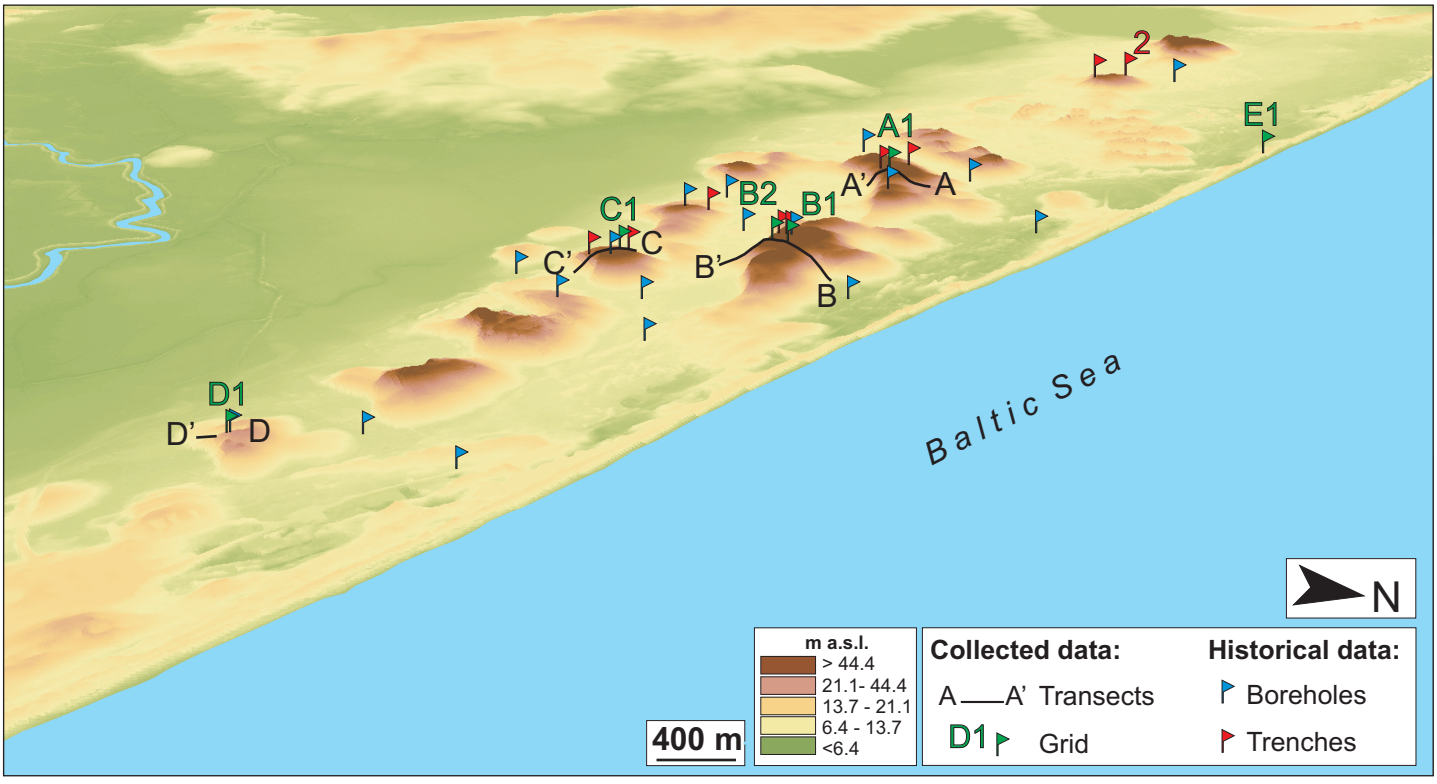
2
E1
A1
A'
A
B2
B1
C1
C
C'
B'
B
D1
D'
D
Baltic Sea
N
400 m
m a.s.l.
> 44.4
21.1- 44.4
13.7 - 21.1
6.4 - 13.7
<6.4
Collected data:
A A' Transects
D1 Grid
Historical data:
Boreholes
Trenches

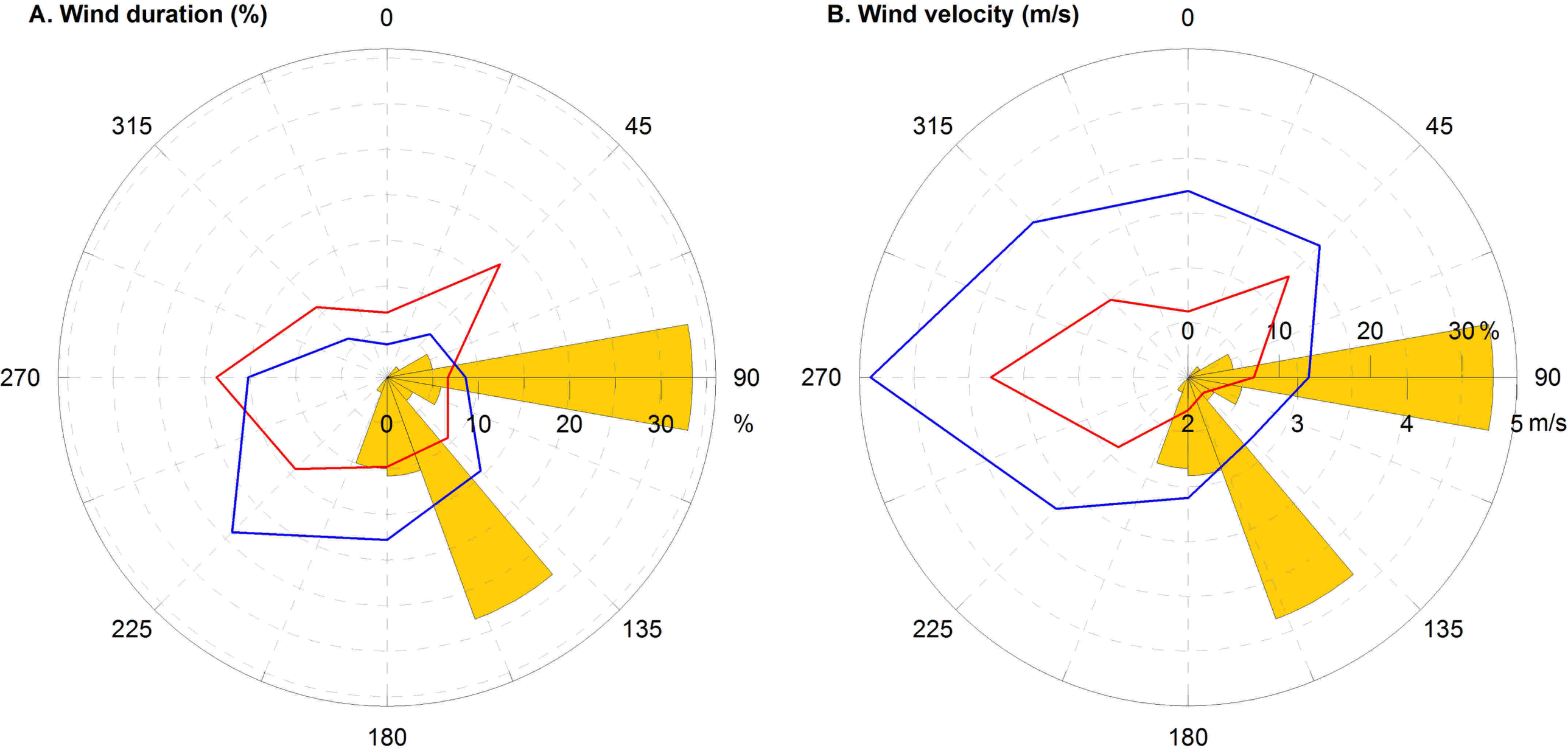
A. Wind duration (%)
0
45
90
135
180
225
270
315
0
10
20
30
%
B. Wind velocity (m/s)
0
45
90
135
180
225
270
315
0
10
20
30 %
2
3
4
5 m/s

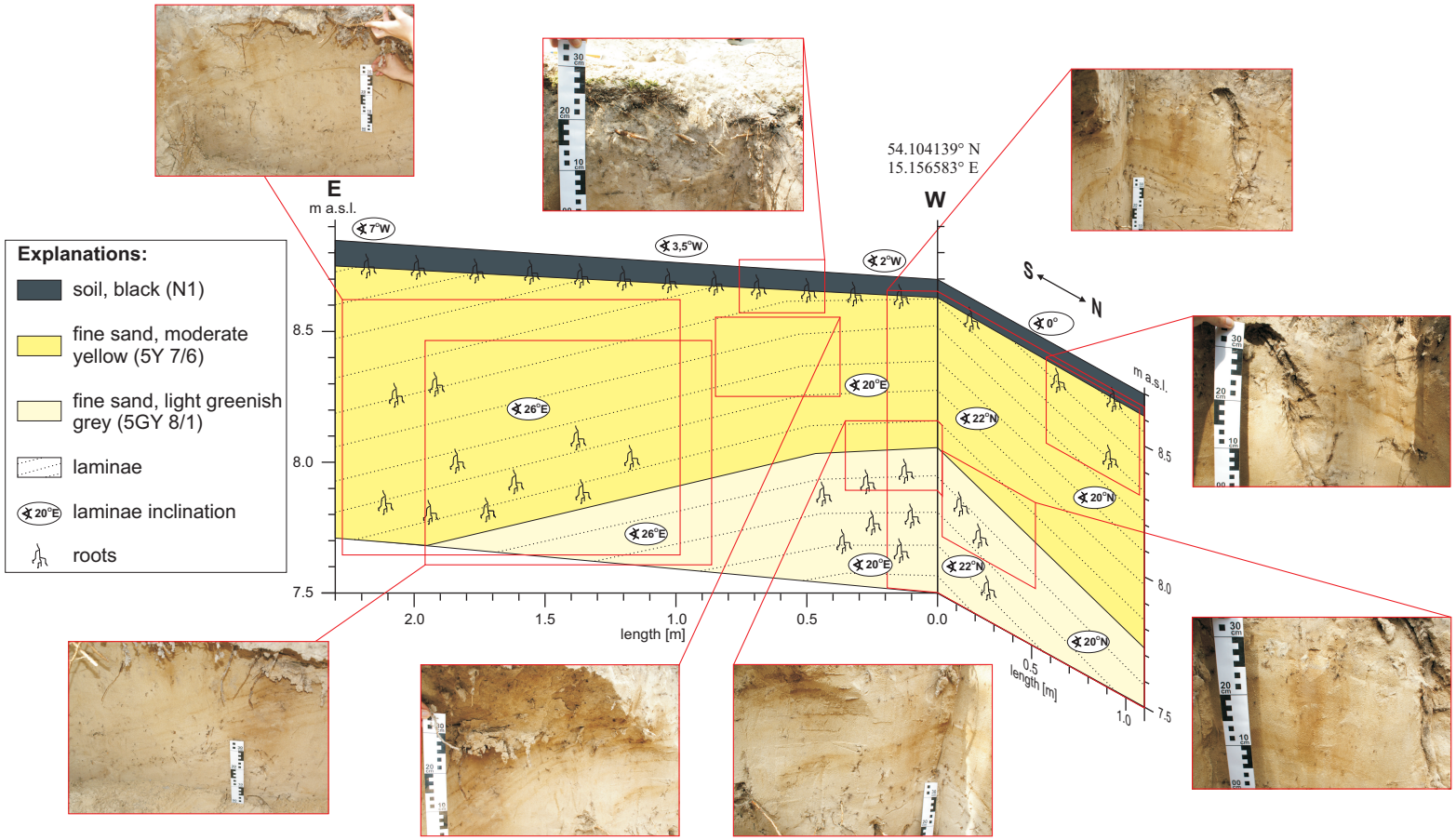
Explanations:
soil, black (N1)
fine sand, moderate yellow (5Y 7/6)
fine sand, light greenish grey (5GY 8/1)
laminae
20°E
laminae inclination
roots
54.104139° N
15.156583° E
E
W
S
N
m a.s.l.
8.5
8.0
7.5
2.0
1.5
1.0
0.5
0.0
length [m]
7°W
3,5°W
2°W
0°
26°E
20°E
22°N
20°N

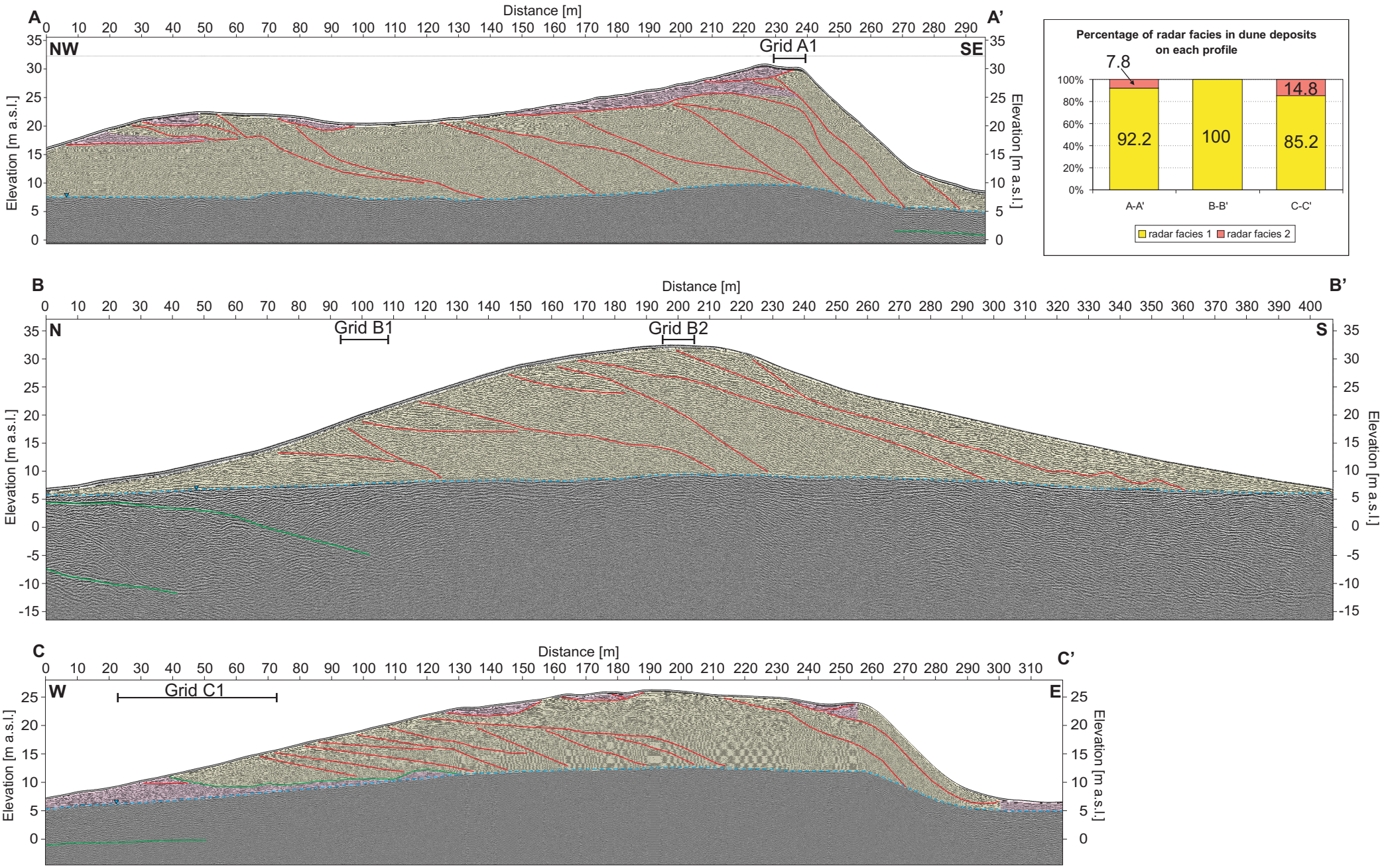
A
A'
NW
SE
Grid A1
Distance [m]
Elevation [m a.s.l.]
B
B'
N
S
Grid B1
Grid B2
C
C'
W
E
Grid C1
Percentage of radar facies in dune deposits on each profile
7.8
92.2
100
14.8
85.2
A-A'
B-B'
C-C'
radar facies 1
radar facies 2

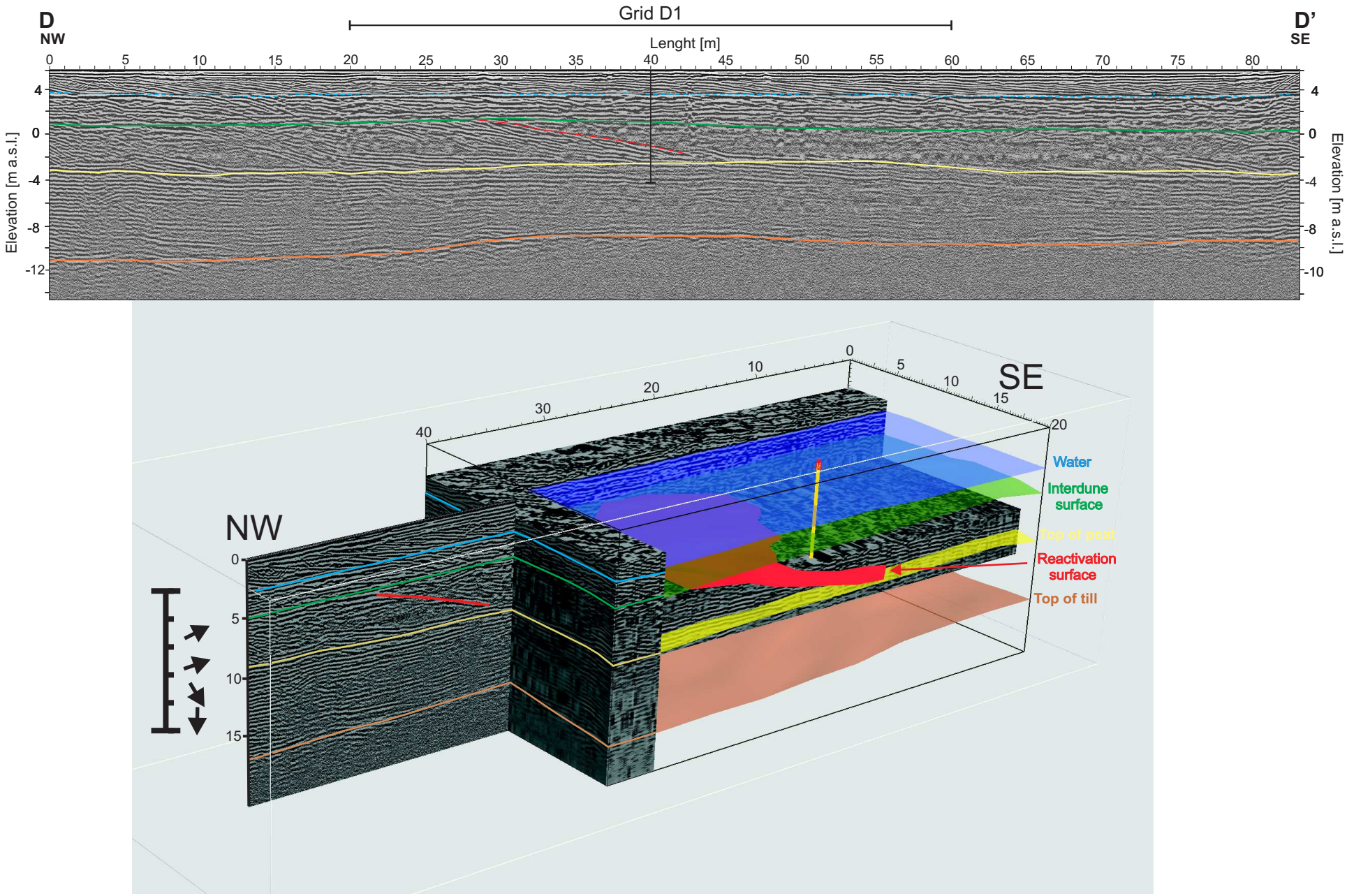
D
NW
Grid D1
D'
SE
Lenght [m]
Elevation [m a.s.l.]
Elevation [m a.s.l.]
NW
SE
Water
Interdune surface
Top of peat
Reactivation surface
Top of till

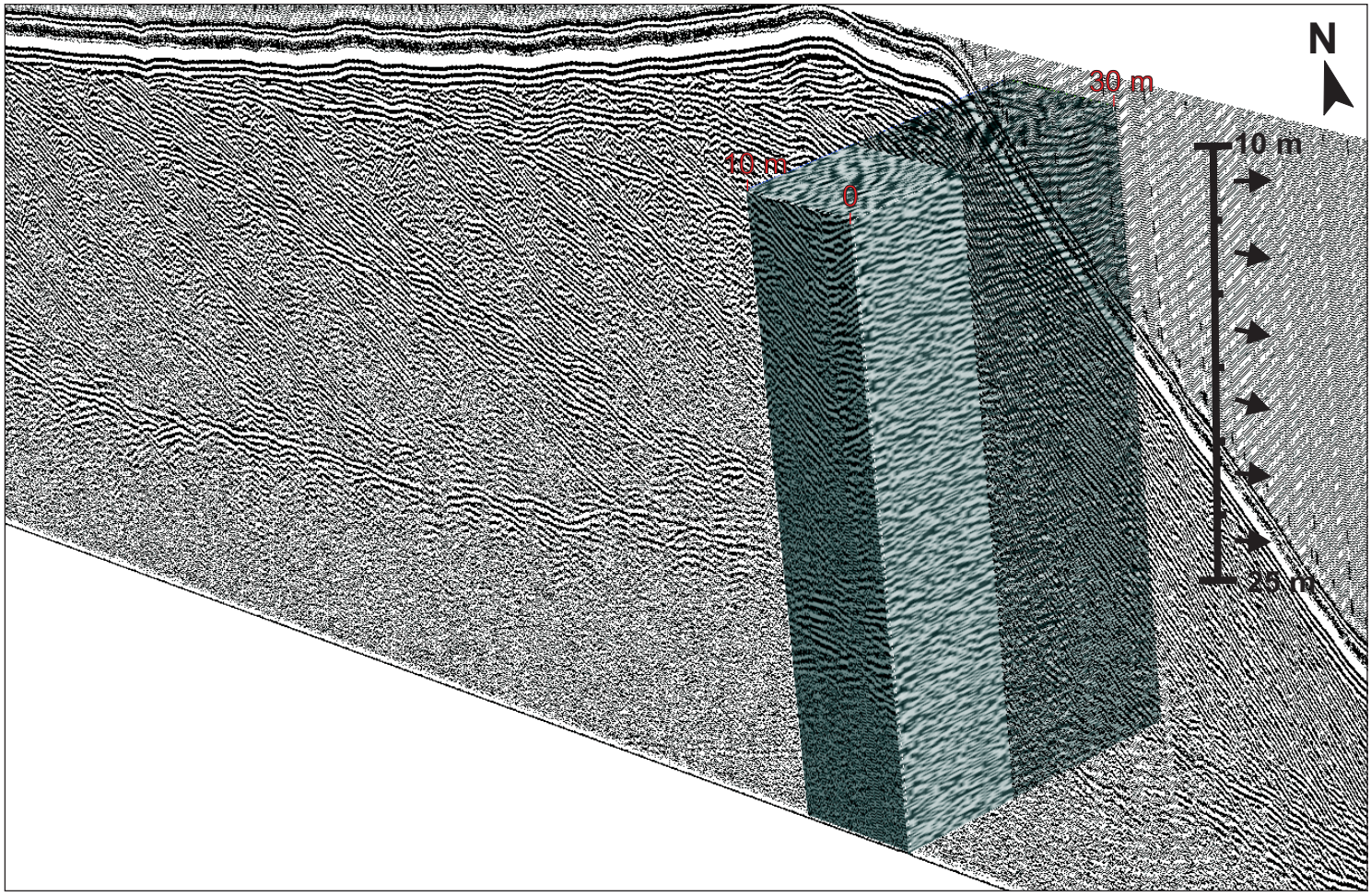
N
30 m
10 m
0
10 m
25 m

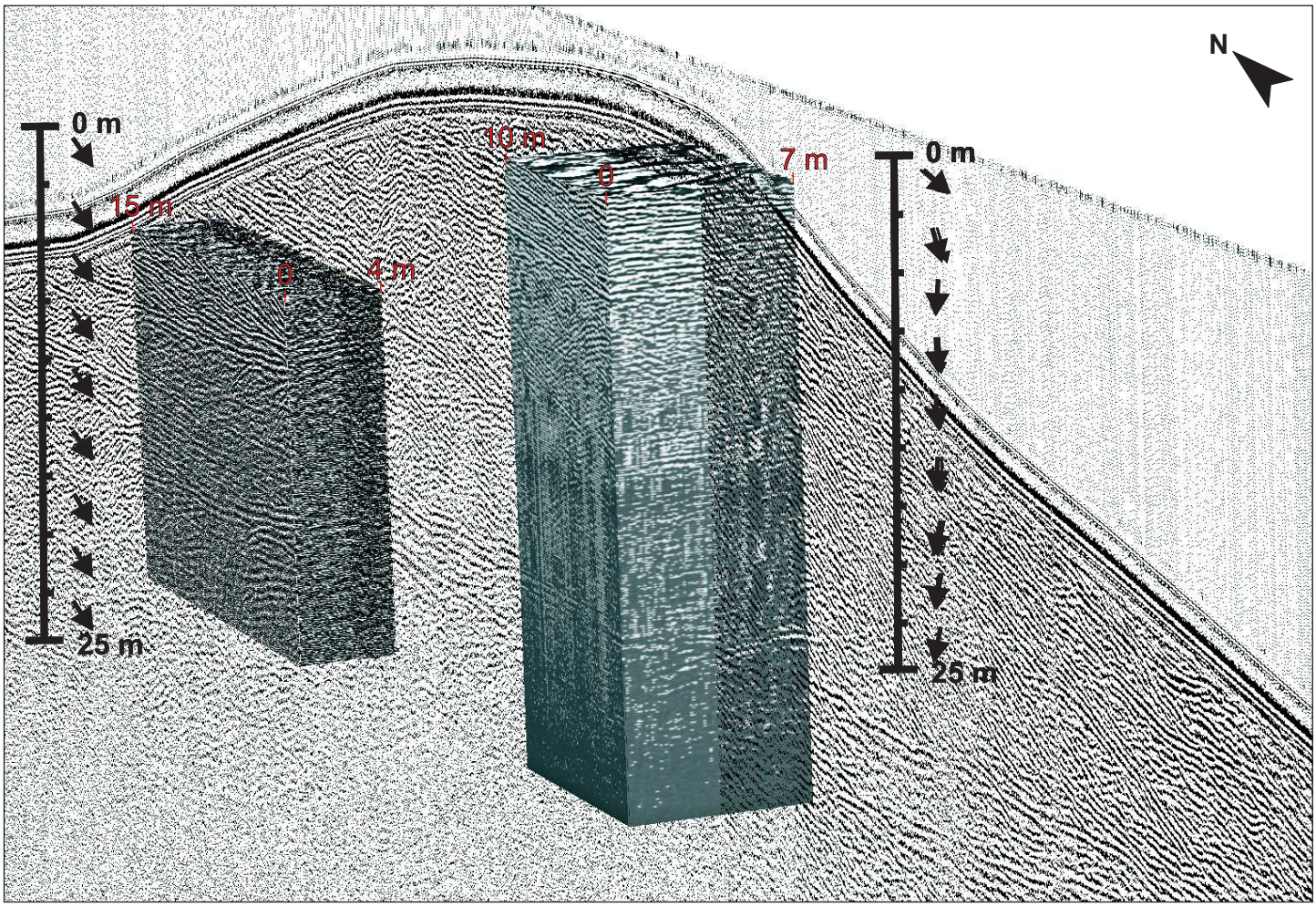
N
0 m
15 m
0
4 m
10 m
0
7 m
0 m
25 m
25 m

Grid E1

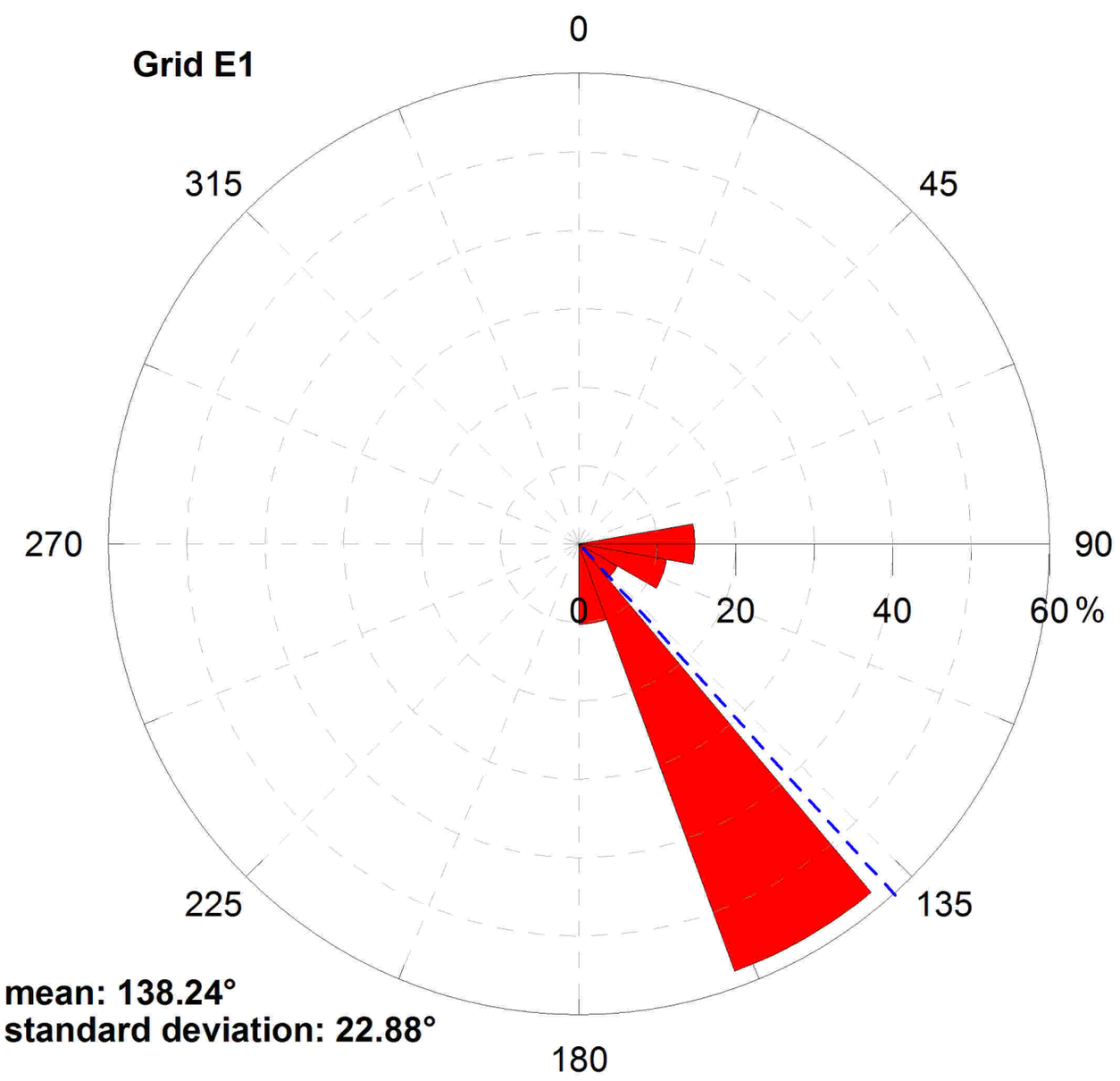

mean: 138.24°
standard deviation: 22.88°

Grid B1

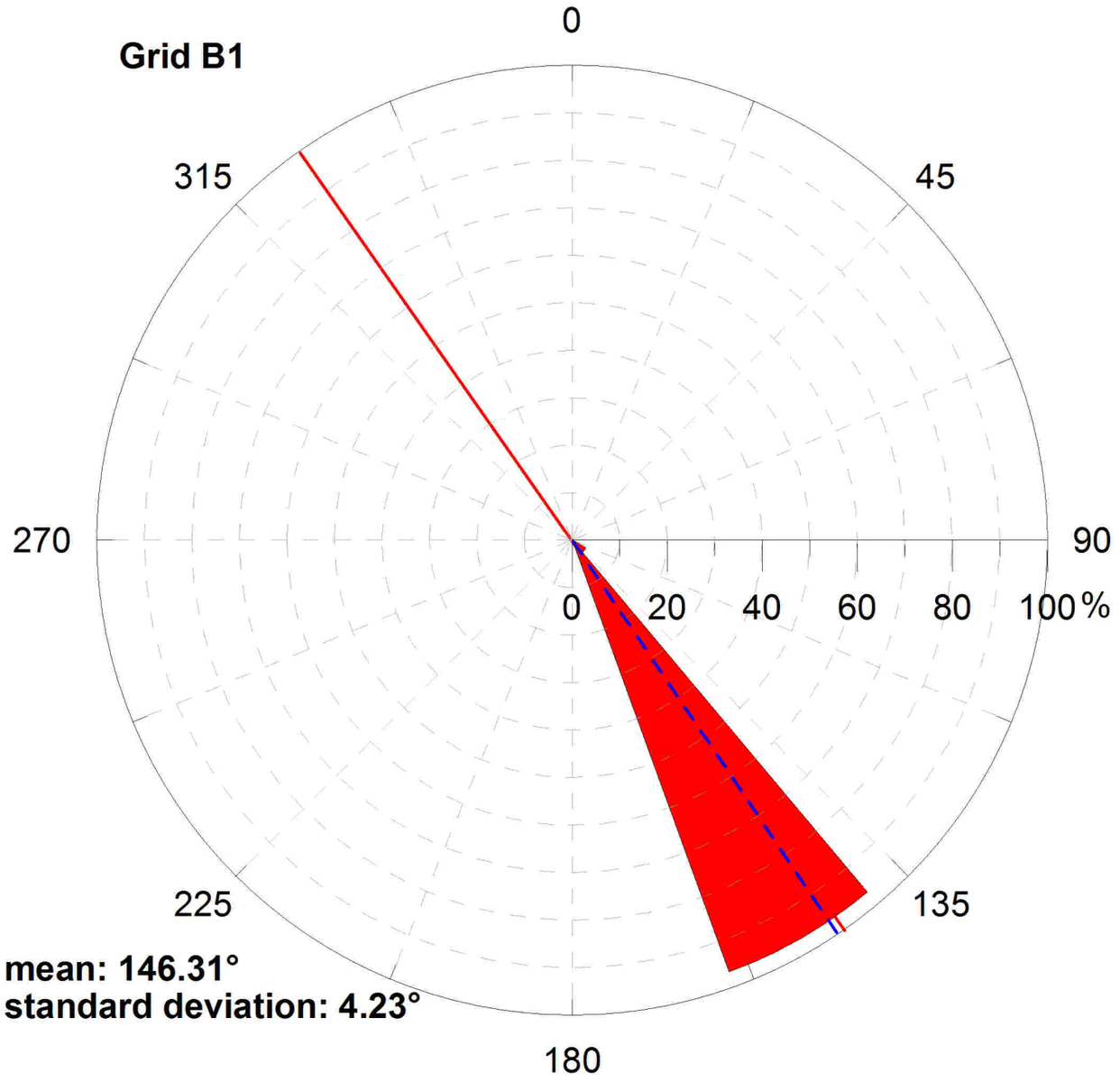

mean: 146.31°
standard deviation: 4.23°

Grid A1

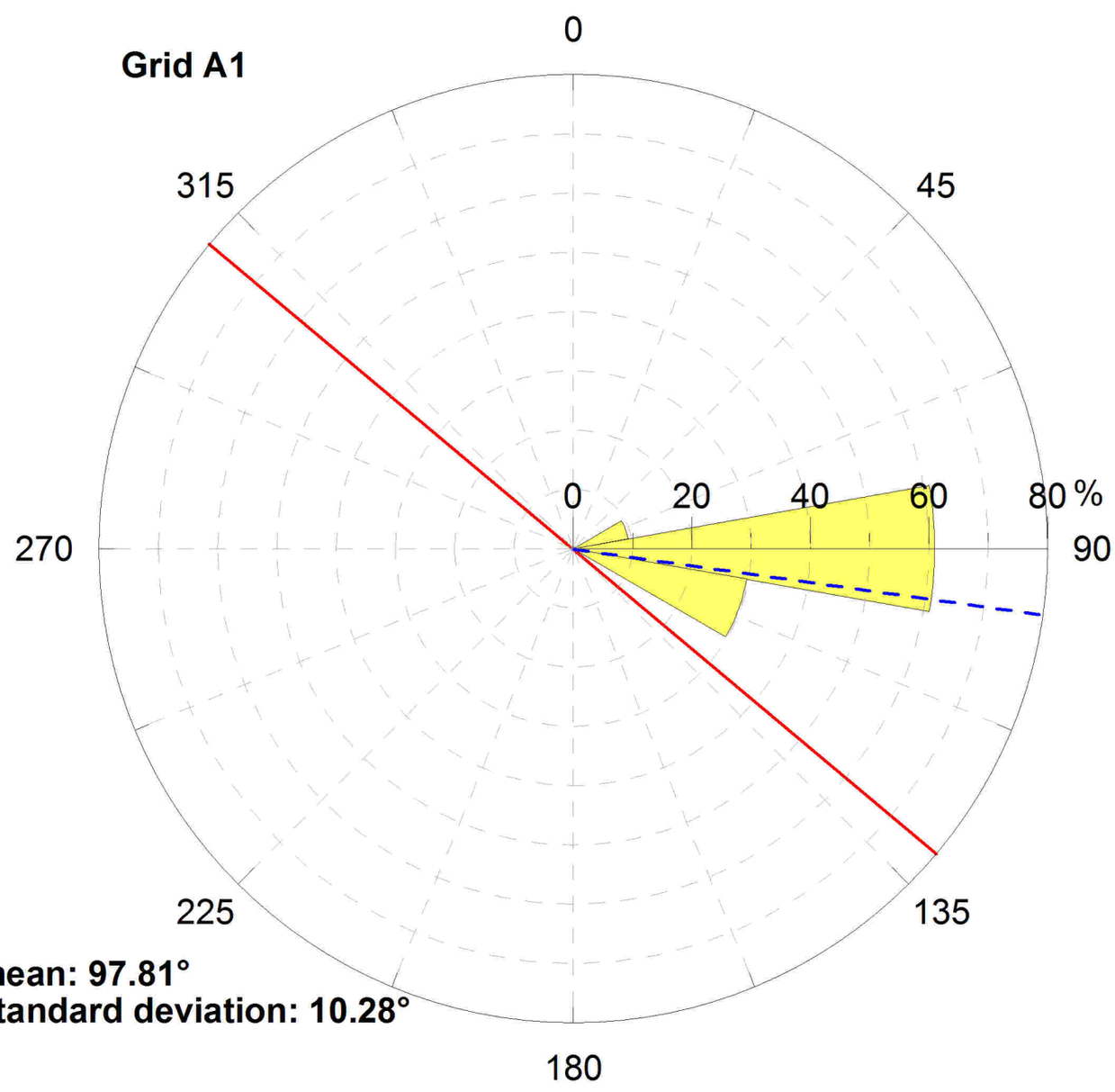

mean: 97.81°
standard deviation: 10.28°

Grid B2

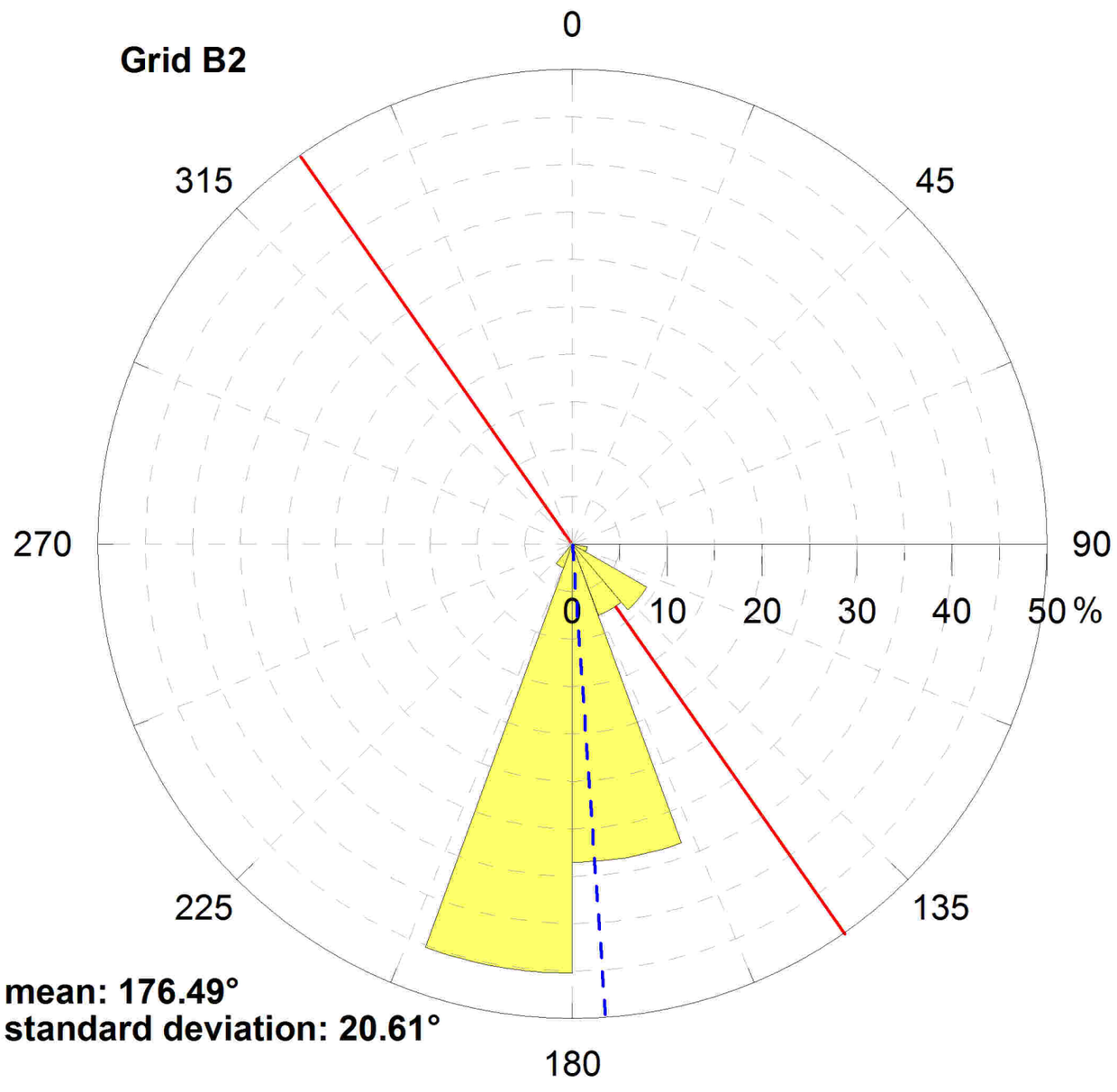

mean: 176.49°
standard deviation: 20.61°

Grid C1

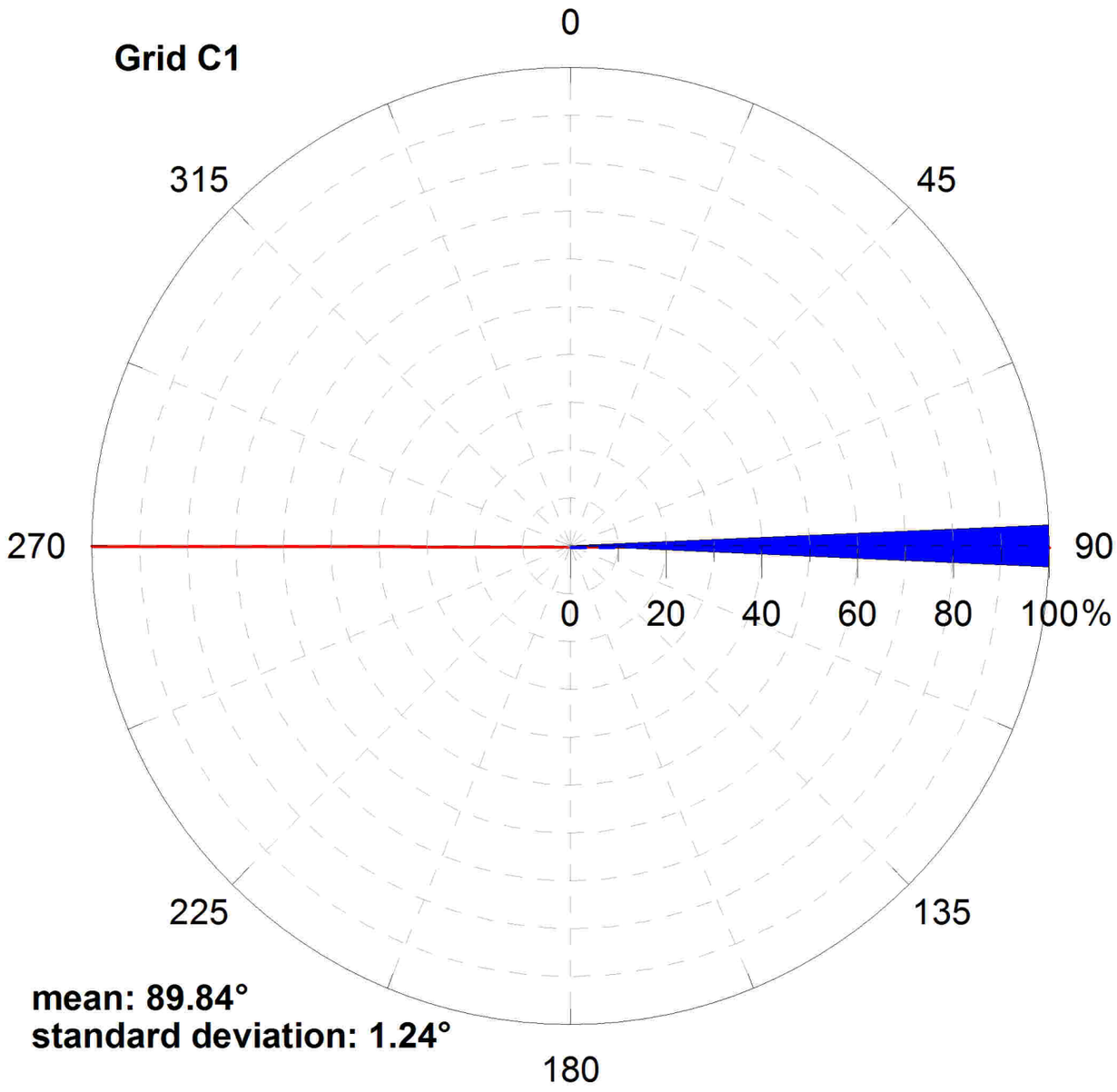

mean: 89.84°
standard deviation: 1.24°

Grid D1

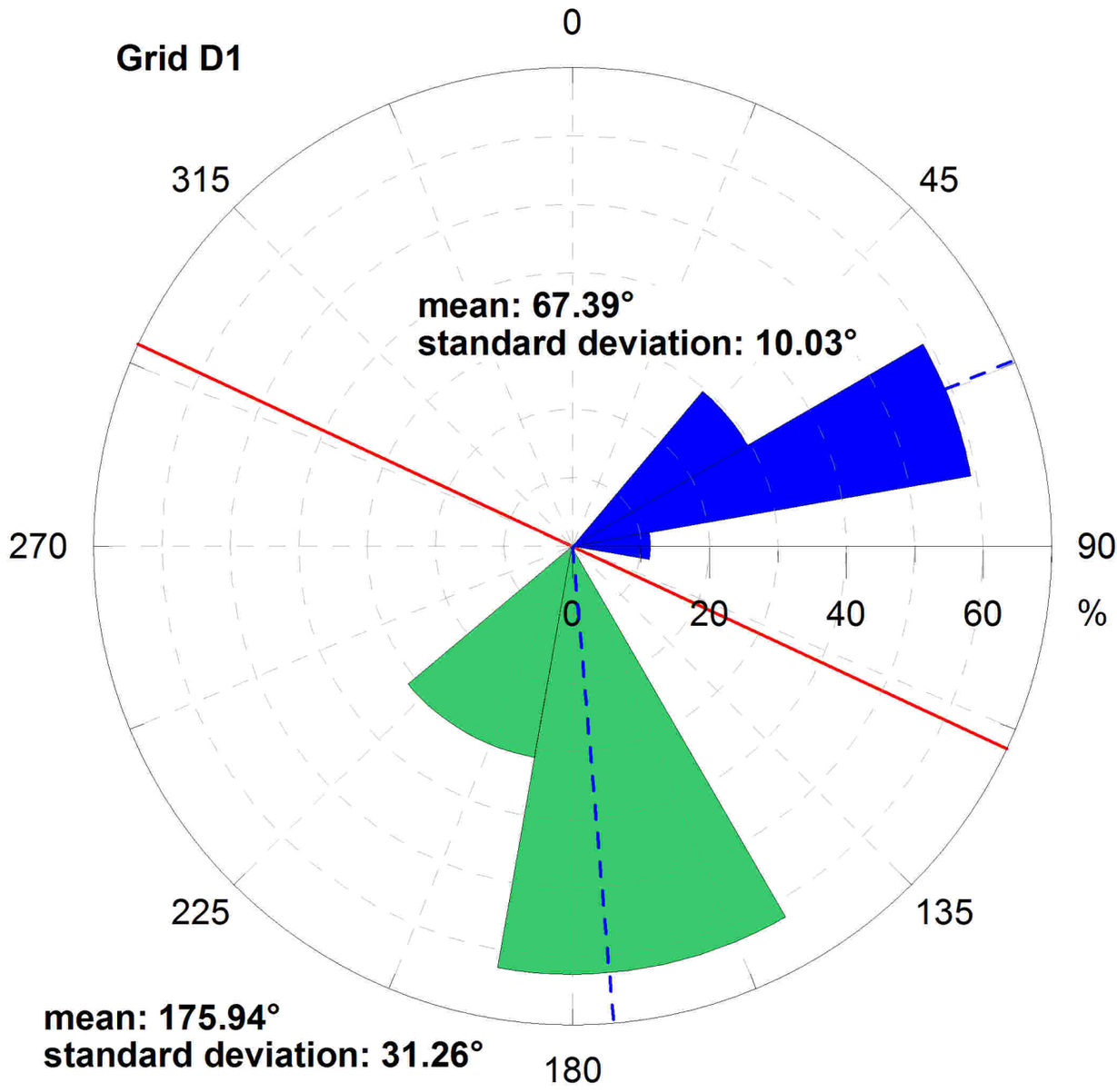

mean: 175.94°
standard deviation: 31.26°

LEGEND
- - - mean direction of inclination
—— transect direction

A

0 0,3 0,6 1,2 1,8 2,4 km

N

Transport directions

- 45°–105°
- 105°–135°
- 135°–200°

Mean: 126°
Standard deviation: 30.9°

Mean: 144°
Standard deviation: 0.8°

mean size: 0.230 mm
sorting: 0.32
skewness: -0.059

mean size: 0.232 mm
sorting: 0.32
skewness: -0.027

mean size: 0.230 mm
sorting: 0.29
skewness: -0.008

Mean: 86°
Standard deviation: 18.1°

B

0 0,3 0,6 1,2 1,8 2,4 km

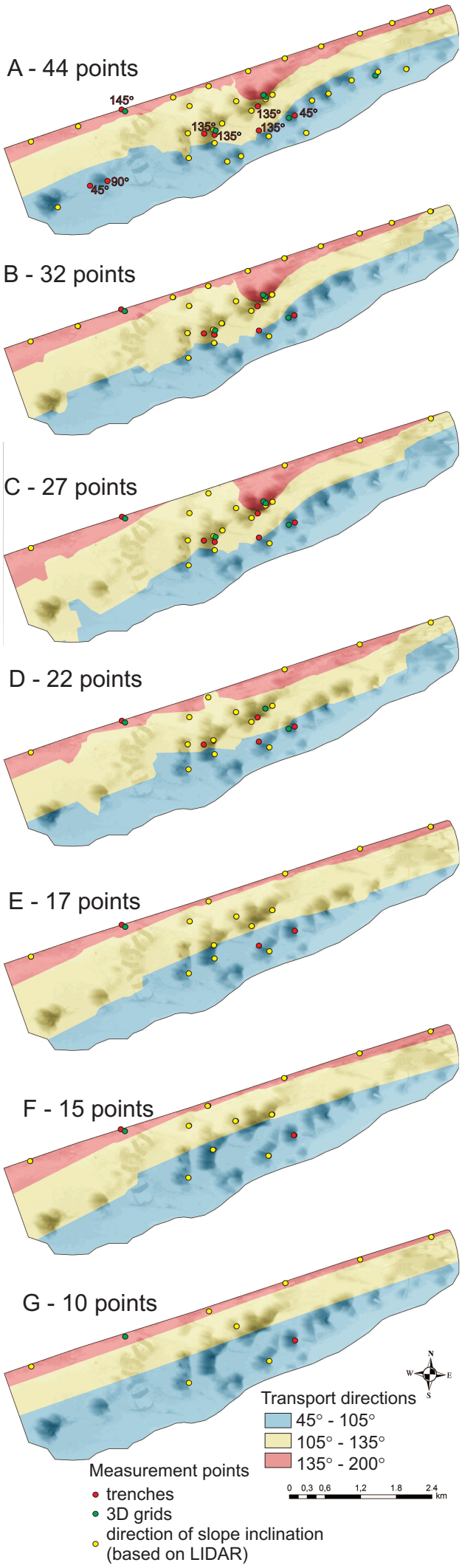
A - 44 points
145°
135°
45°
135°
135°
135°
45°
90°
B - 32 points
C - 27 points
D - 22 points
E - 17 points
F - 15 points
G - 10 points
N
W
E
S
Transport directions
45° - 105°
105° - 135°
135° - 200°
0 0,3 0,6 1,2 1.8 2.4 km
Measurement points
trenches
3D grids
direction of slope inclination
(based on LIDAR)

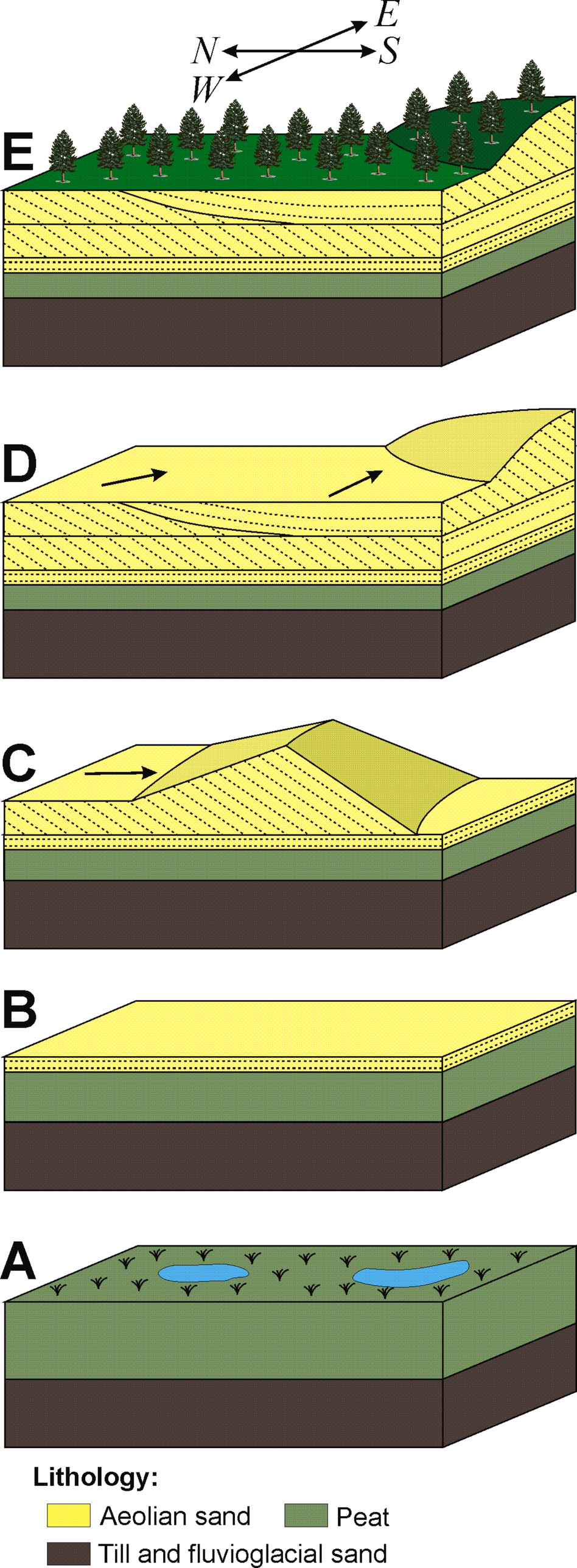
E
N
S
W
E
D
C
B
A
Lithology:
Aeolian sand
Peat
Till and fluvioglacial sand